Boundary-Layer Meteorol (2012) 145:249–272
DOI 10.1007/s10546-011-9685-2

ARTICLE

Analytical and Numerical Investigation of Two-Dimensional Katabatic Flow Resulting from Local Surface Cooling

Alan Shapiro · Bryan Burkholder · Evgeni Fedorovich

Received: 2 May 2011 / Accepted: 30 November 2011 / Published online: 28 December 2011

Abstract The analysis of katabatic flows is often complicated by heterogeneity in surface characteristics. This study focuses on an idealized type of katabatic flow driven by a simple form of inhomogeneous surface forcing: a buoyancy or buoyancy flux that varies down the slope as a top-hat profile (cold strip). We consider the two-dimensional Boussinesq system of governing flow equations with the slope angle, Brunt–Väisälä frequency, and coefficients of eddy viscosity and diffusivity treated as constants. The steady-state problem is solved analytically in a linearized boundary-layer framework. Key flow structures are a primary katabatic jet (essentially the classical one-dimensional Prandtl jet), a rotor-like feature straddling the upslope end of the strip, and two nearly horizontal jets: an inward jet of environmental air feeding into the primary jet on the upslope end of the strip and an outward jet resulting from the intrusion of the primary katabatic jet into the environment on the downslope end of the strip. Next, the corresponding nonlinear initial value problem is solved numerically until a steady state is reached at low levels. The main features of the linear solution are seen in the numerical results, but with some notable differences: (i) the primary jet in the numerical simulation requires a longer distance to attain a one-dimensional boundary-layer structure and extends further downslope off the strip before intruding into the environment; (ii) the numerically simulated outward environmental jet is narrower and more intense than the inward jet, and has a pronounced wave-like structure.

Keywords Buoyancy · Buoyancy flux · Inhomogeneous surface · Katabatic flow · Stable stratification

A. Shapiro (✉) · B. Burkholder · E. Fedorovich
School of Meteorology, University of Oklahoma, 120 David L. Boren Blvd., Room 5900, Norman, OK 73072, USA
e-mail: ashapiro@ou.edu

A. Shapiro
Center for Analysis and Prediction of Storms, University of Oklahoma, Norman, OK, USA

1 Introduction

When a sloping surface is cooled, a temperature contrast is set up between an air parcel near the surface and the environmental air at the same elevation as the parcel. The buoyancy force associated with this contrast projects in the along-slope direction and induces a flow, commonly called the katabatic wind, that is directed downslope. The counterpart of the katabatic wind in the case of sloping surface heating is the upslope anabatic wind. Slope winds of both types are ubiquitous in complex terrain, especially when synoptic-scale forcing is weak (Atkinson 1981; Mahrt and Larsen 1982; Vergeiner and Dreiseitl 1987; Whiteman 1990, 2000; Mahrt et al. 2001; Poulos and Zhong 2008). They exert a vital influence on weather and climate, with impacts on air quality, agriculture, recreation, and fire management (Dickerson and Gudiksen 1983; Broder and Gygax 1985; Sturman 1987; King et al. 1987; Segal et al. 1988; Nappo et al. 1989; Low 1990; Banta et al. 1996, 1997; Bossert 1997; Millán et al. 1998; Hernández et al. 1998; Fernando et al. 2001; Barros et al. 2003; Lee et al. 2003; Kossmann and Sturman 2004; Finn et al. 2008; Sharples 2009; Gohm et al. 2009; Fernando 2010).

An early milestone in the theory of slope flows was the Prandtl (1942) model of one-dimensional slope flows. Prandtl solved the equations of motion and thermal energy for the steady flow of a viscous fluid along a uniformly cooled (or heated) planar surface in a stably stratified environment. In the original model, the surface forcing was specified in terms of a temperature (buoyancy) disturbance. The solution was characterized by a low-level jet capped by a weak return flow, while the buoyancy decayed rapidly in magnitude away from the slope and changed sign in the return flow aloft. This model compared qualitatively well with observations when the mixing parameters were appropriately tuned (Tyson 1968; Hootman and Blumen 1983; Clements et al. 1989; Papadopoulos et al. 1997; Oerlemans 1998) or prescribed as height-dependent parameters (Grisogono and Oerlemans 2001). Flow profiles corresponding to the Prandtl solutions have also been found in the analytical and numerical studies of natural convection along a heated vertical wall immersed in a stably stratified fluid (Shapiro and Fedorovich 2004a,b) and in a version of the Prandtl model with the surface forcing specified in terms of the heat (buoyancy) flux (Fedorovich and Shapiro 2009a).

Analyses of real katabatic flows are complicated by complex basin geometries, interactions with synoptic-scale flows, the presence of surface inhomogeneities arising from topographic shading (e.g., upper slopes are shaded, while lower slopes are exposed to the sun), variations in snow, ice, soil cover, soil moisture, cloud cover, or vegetation type, and the fact that these flows are generally turbulent. Therefore, it may be unrealistic to expect a theory to provide a satisfactory explanation of a slope flow observed at a specific location on a particular day. However, useful insights may be gained into slope-flow phenomena by studying idealized flows and focusing on individual aspects of the general problem. Two noteworthy studies along those lines are the Egger (1981) and Kondo (1984) analyses of slope flows driven by an inhomogeneous surface forcing. Their analyses can be thought of as two-dimensional extensions of the Prandtl model.

Egger (1981) and Kondo (1984) considered the linearized governing equations for the case where a planar slope is subject to a top-hat distribution of slope buoyancy (a cold or hot surface strip running across the slope). The buoyancy varied down the slope but was constant in the cross-slope direction [the sister problem of a downslope running cold strip was treated by Axelsen et al. (2010)]. Their analyses revealed that the primary slope wind was connected to twin environmental jets, one directed horizontally towards the slope and feeding into the boundary layer, and one leaving the boundary layer and directed horizontally into the envi-

ronment. Horizontally directed ejections from sloping boundaries are frequently observed in valleys and basins, where they affect air quality (Vergeiner and Dreiseitl 1987; Lu and Turco 1994; Soriano et al. 2001; Fernando et al. 2001; Monti et al. 2002; Barros et al. 2003; Lee et al. 2003; Gohm et al. 2009; Lehner and Gohm 2010). A far-propagating environmental response to inhomogeneous forcing was also noted in Shapiro and Fedorovich (2007), where an accelerating katabatic jet induced by linearly varying surface buoyancy down the slope led to the formation of horizontal environmental jets that entered/left the katabatic boundary layer. Similar jets were found in the numerical study of Burkholder et al. (2009).

This paper revisits the problem of two-dimensional katabatic flow driven by surface forcings that vary downslope locally, as in Egger (1981), Kondo (1984), and Burkholder et al. (2009). In Sect. 2 we present the linearized governing equations and show that a katabatic flow driven by top-hat surface cooling is controlled by a single parameter—a non-dimensional strip width. The governing equations are solved by Fourier methods in Sect. 3, and examples are considered in Sect. 4. By including many Fourier components in the solution (10^6 compared with 20 in Egger's analysis), we obtain a high-resolution view of flows across a range of strip widths. In Sect. 5 we extend the numerical analysis of Burkholder et al. (2009) using a parallel version of the code used in that study. Simulating the flow in a very large domain (to maximally delay effects of lateral boundaries) and with high resolution allows us to explore nonlinear aspects of the problem. A summary follows in Sect. 6.

2 Governing Equations

We work in a slope-following right-hand Cartesian coordinate system (Fig. 1) with the X axis directed downslope at an angle α to the horizontal coordinate X^*, and Z axis directed perpendicular to the slope. The slope coincides with the surface $Z = 0$. All flow variables are independent of the cross-slope (Y, into page) coordinate. With the Coriolis force neglected, the velocity vector has only along-slope and slope-normal components, U and W, respectively. For future reference, we note from Fig. 1 that on surfaces of constant elevation, the following relation holds: $Z = X \tan\alpha + \text{const}$.

The Boussinesq governing equations for two-dimensional flow of a stably stratified non-rotating fluid above a planar slope were presented in Shapiro and Fedorovich (2007). We consider here the linearized boundary-layer version of those equations (X-derivatives neglected in stress and diffusion terms; quasi-hydrostatic approximation made in slope-normal equation of motion) in the steady state:

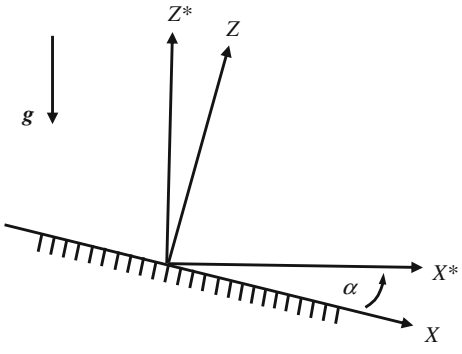

Fig. 1 Slope-following coordinate system. The along-slope (X) and slope-normal (Z) coordinates are inclined at an angle α to the horizontal (X^*) and vertical (Z^*) coordinates, respectively. Flow variables are independent of the cross-slope coordinate (Y), which points into the page

$$0 = -\frac{\partial \Pi}{\partial X} - B\sin\alpha + \nu\frac{\partial^2 U}{\partial Z^2}, \tag{1}$$

$$0 = -\frac{\partial \Pi}{\partial Z} + B\cos\alpha, \tag{2}$$

$$0 = UN^2\sin\alpha - WN^2\cos\alpha + \kappa\frac{\partial^2 B}{\partial Z^2}, \tag{3}$$

$$\frac{\partial U}{\partial X} + \frac{\partial W}{\partial Z} = 0. \tag{4}$$

Here (1) is the along-slope equation of motion, (2) is the equation for quasi-hydrostatic equilibrium, applicability of which to slope flows is discussed by Mahrt (1982) and Haiden (2003), (3) is the thermal energy equation, and (4) is the mass conservation equation. The normalized pressure perturbation $\Pi \equiv (P - P_\infty)/\rho_\mathrm{r}$ is the difference between the pressure P and the (hydrostatic) environmental pressure P_∞, divided by a constant reference density ρ_r. The buoyancy $B \equiv \beta(\Theta - \Theta_\infty)$ is the difference between the potential temperature Θ and the environmental potential temperature Θ_∞ multiplied by a buoyancy parameter $\beta \equiv g/\Theta_\mathrm{r}$, where Θ_r is a constant reference potential temperature, and g is the acceleration due to gravity. We assume that Θ_∞ increases linearly with the vertical coordinate Z^*, so that the environment is stably stratified ($\mathrm{d}\Theta_\infty/\mathrm{d}Z^* > 0$) with constant Brunt–Väisälä frequency $N \equiv \sqrt{(g/\Theta_\mathrm{r})\mathrm{d}\Theta_\infty/\mathrm{d}Z^*}$. The coefficients of eddy viscosity ν and thermal diffusivity κ are also considered constant.

The lower boundary conditions are the no-slip condition, $U(X,0) = 0$, the impermeability condition, $W(X,0) = 0$, and a specified distribution of buoyancy, $B(X,0) = f(X)$, or of slope-normal buoyancy gradient, $\partial B/\partial Z(X,0) = g(X)$. For brevity we refer to this latter condition as the buoyancy flux condition, even though the actual surface buoyancy flux is $-\kappa\partial B/\partial Z(X,0)$. All the dependent variables are considered to vanish as $|X| \to \infty$ (a necessary condition for the variables to be Fourier-transformable in X) and be bounded as $Z \to \infty$.

To obtain a problem with as few degrees of freedom as possible, we introduce the non-dimensional variables

$$x \equiv \frac{X}{X_\mathrm{s}}, \quad z \equiv \frac{Z}{Z_\mathrm{s}}, \quad u \equiv \frac{U}{U_\mathrm{s}}, \quad w \equiv \frac{W}{W_\mathrm{s}}, \quad \pi \equiv \frac{\Pi}{\Pi_\mathrm{s}}, \quad b \equiv \frac{B}{B_\mathrm{s}}, \tag{5}$$

where

$$Z_\mathrm{s} \equiv \frac{(\nu\kappa)^{1/4}}{(N\sin\alpha)^{1/2}}, \quad X_\mathrm{s} \equiv \frac{(\nu\kappa)^{1/4}\cos\alpha}{N^{1/2}\sin^{3/2}\alpha},$$
$$U_\mathrm{s} \equiv \frac{B_\mathrm{s}}{N}\left(\frac{\kappa}{\nu}\right)^{1/2}, \quad W_\mathrm{s} \equiv \frac{B_\mathrm{s}}{N}\left(\frac{\kappa}{\nu}\right)^{1/2}\frac{\sin\alpha}{\cos\alpha}, \quad \Pi_\mathrm{s} \equiv \frac{B_\mathrm{s}(\nu\kappa)^{1/4}\cos\alpha}{(N\sin\alpha)^{1/2}}, \tag{6}$$

and B_s (> 0) is the peak magnitude of the surface buoyancy (if buoyancy is specified) or the normalized buoyancy gradient (if buoyancy flux is specified),

$$B_\mathrm{s} \equiv \begin{cases} \max\limits_{X\in(-\infty,\infty)} |B(X,0)|\,, & \text{(if buoyancy is specified),} \\ \max\limits_{X\in(-\infty,\infty)} \left|Z_\mathrm{s}\frac{\partial B}{\partial Z}(X,0)\right|, & \text{(if buoyancy flux is specified).} \end{cases} \tag{7}$$

Apart from notational differences and $O(1)$ numerical factors, the Z_s and U_s defined in (6) are, respectively, the boundary-layer thickness and along-slope velocity scales in the Prandtl (1942) slope flow model. In terms of these two Prandtl scales, the other scales in (6) can be written as

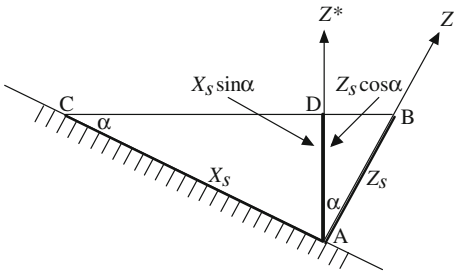

Fig. 2 Schematic illustration of the length-scale relation $X_\mathrm{s} \equiv Z_\mathrm{s} \cot\alpha$. The slope-normal length scale Z_s is the thickness of the boundary layer in the one-dimensional (Prandtl) model. The along-slope length scale X_s is the distance along the slope over which the elevation changes by the same amount as over the slope-normal distance Z_s. Since the elevation change from A to C ($\Delta Z^* = X_\mathrm{s} \sin\alpha$) is the same as from A to B ($\Delta Z^* = Z_\mathrm{s} \cos\alpha$), $X_\mathrm{s} = Z_\mathrm{s} \cot\alpha$

$$X_\mathrm{s} \equiv Z_\mathrm{s} \cot\alpha, \tag{8a}$$

$$W_\mathrm{s} \equiv U_\mathrm{s} \tan\alpha, \tag{8b}$$

$$\Pi_\mathrm{s} \equiv B_\mathrm{s} Z_\mathrm{s} \cos\alpha. \tag{8c}$$

As seen in Fig. 2, X_s is the distance along the slope over which the elevation change is equal to the depth scale of the Prandtl boundary layer Z_s.

The non-dimensional versions of (1)–(4) are

$$0 = -\frac{\partial \pi}{\partial x} - b + \frac{\partial^2 u}{\partial z^2}, \tag{9}$$

$$0 = -\frac{\partial \pi}{\partial z} + b, \tag{10}$$

$$0 = u - w + \frac{\partial^2 b}{\partial z^2}, \tag{11}$$

$$\frac{\partial u}{\partial x} + \frac{\partial w}{\partial z} = 0. \tag{12}$$

These equations have been cleared of all parameters—even non-dimensional parameters such as the slope angle or Prandtl number. Accordingly, the only free parameters in the non-dimensional problem are those associated with the thermal state of the slope. In the simple case, where the surface buoyancy or buoyancy flux are top-hat functions of x with non-zero values confined to a strip of dimensional length L (considered in Sect. 4), the non-dimensional surface buoyancy or slope-normal buoyancy gradient has a peak magnitude of unity. Thus, the resulting local flows are fully characterized by a single parameter—the non-dimensional strip width

$$l \equiv \frac{L}{X_\mathrm{s}} = L \frac{N^{1/2} \sin^{3/2}\alpha}{(\nu\kappa)^{1/4} \cos\alpha}. \tag{13}$$

In view of the above interpretation of X_s, we see that $l < 1$ and $l > 1$ correspond to strips whose elevation changes are, respectively, within one Prandtl boundary-layer thickness and in excess of one Prandtl boundary-layer thickness.

3 Fourier Analysis

With u and w eliminated in favor of a streamfunction ψ defined through

$$u = \frac{\partial \psi}{\partial z}, \tag{14a}$$

$$w = -\frac{\partial \psi}{\partial x}, \tag{14b}$$

Equation 12 is satisfied identically, while Eq. 11 becomes

$$0 = \frac{\partial \psi}{\partial x} + \frac{\partial \psi}{\partial z} + \frac{\partial^2 b}{\partial z^2}. \tag{15}$$

Eliminating π by taking $\partial/\partial z$ (Eq. 9) $- \partial/\partial x$ (Eq. 10) yields a linear boundary-layer form of cross-slope (Y-component) vorticity equation,

$$0 = -\frac{\partial b}{\partial x} - \frac{\partial b}{\partial z} + \frac{\partial^4 \psi}{\partial z^4}. \tag{16}$$

Taken together, the first two terms in (16) describe the change in buoyancy along a surface of constant elevation, $-\partial b/\partial x - \partial b/\partial z = -\partial b/\partial x^*$ where $x^* \equiv X^*/X_s$. Thus (16) expresses a balance between the baroclinic generation of cross-slope vorticity and the slope-normal diffusion of cross-slope vorticity.

Eliminating b from (15) and (16) yields

$$\frac{\partial^2 \psi}{\partial x^2} + 2\frac{\partial^2 \psi}{\partial x \partial z} + \frac{\partial^2 \psi}{\partial z^2} + \frac{\partial^6 \psi}{\partial z^6} = 0. \tag{17}$$

We solve (17) by the method of Fourier transforms (Mathews and Walker 1970). Multiplying (17) by e^{-ikx}, integrating the result from $x = -\infty$ to $x = \infty$, and setting ψ to vanish as $|x| \to \infty$, we obtain

$$\frac{d^6 \hat{\psi}}{dz^6} + \frac{d^2 \hat{\psi}}{dz^2} + 2ik\frac{d\hat{\psi}}{dz} - k^2 \hat{\psi} = 0, \tag{18}$$

where $\hat{\psi}$ is the Fourier transform of ψ. The transform and its inverse (which is ψ) are related as

$$\psi(x, z) = \frac{1}{\sqrt{2\pi}} \int_{-\infty}^{\infty} e^{ikx} \hat{\psi}(k, z) dk, \tag{19}$$

$$\hat{\psi}(k, z) = \frac{1}{\sqrt{2\pi}} \int_{-\infty}^{\infty} e^{-ikx} \psi(x, z) dx. \tag{20}$$

Applying the trial solution $\hat{\psi} \sim e^{mz}$ in (18) yields the polynomial equation,

$$m^6 = -(ik + m)^2. \tag{21}$$

Taking the square root of (21) yields the two cubic equations:

$$m^3 = \pm(im - k). \tag{22}$$

Thus, the solutions of (21) are the three solutions of (22) corresponding to the plus sign together with the three solutions corresponding to the minus sign. Of these solutions, those

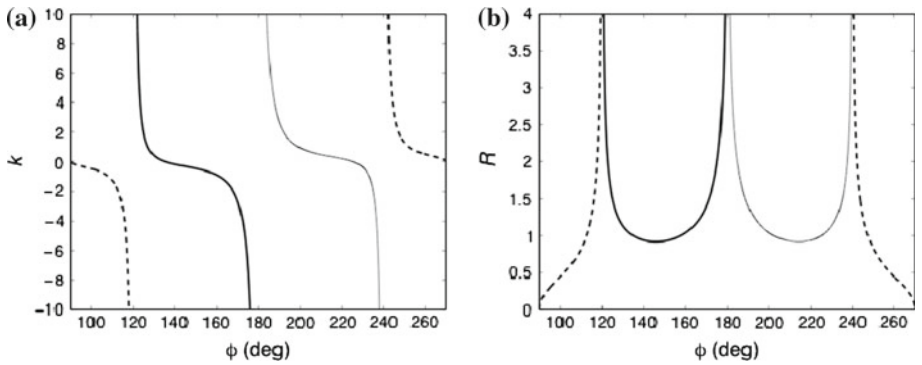

Fig. 3 Implicit (parametric) solutions of Eq. 22: **a** wavenumber $k_j(\phi)$ and **b** amplitude $R_j(\phi)$ functions for the three physically acceptable solutions. *Thin solid lines* display the $j = 1$ solution, which corresponds to $s_1(\phi) = 1$. *Bold solid lines* display the $j = 2$ solution, which corresponds to $s_2(\phi) = -1$. *Bold dashed lines* display the $j = 3$ solution, which corresponds to $s_3(\phi) = 1$ for $90° < \phi < 120°$ and to $s_3(\phi) = -1$ for $240° < \phi < 270°$

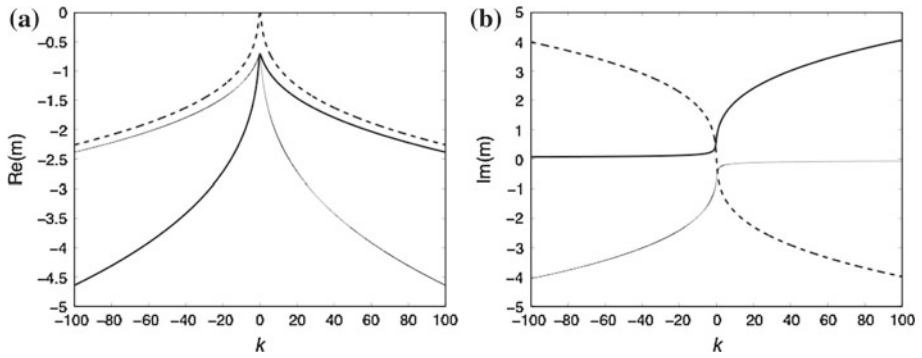

Fig. 4 Real, (**a**), and imaginary, (**b**), parts of the three physically acceptable solutions $m_j(k)$ of Eq. 22. *Thin solid line* corresponds to the $j = 1$ solution. *Bold solid line* corresponds to the $j = 2$ solution. *Bold dashed line* corresponds to the $j = 3$ solution

with positive real parts must be rejected to avoid blow-up of $\hat{\psi}$ (and ψ) far above the slope. The physically acceptable solutions are derived in Appendix A (Figs. 3, 4). Denoting these solutions by m_1, m_2 and m_3, the general solution for $\hat{\psi}$ can be written as

$$\hat{\psi} = n_1 \mathrm{e}^{m_1 z} + n_2 \mathrm{e}^{m_2 z} + n_3 \mathrm{e}^{m_3 z}, \tag{23}$$

where the constants $n_1, n_2,$ and n_3 are to be fixed by the boundary conditions.

It can be shown that b also satisfies (17), and so its Fourier transform $\hat{b}$ has the form of (23), but with a different set of multiplicative constants. After relating these constants to $n_1, n_2,$ and n_3 by considering the Fourier-transformed version of (15), we obtain

$$\hat{b} = -(m_1 + ik)\frac{n_1}{m_1^2}\mathrm{e}^{m_1 z} - (m_2 + ik)\frac{n_2}{m_2^2}\mathrm{e}^{m_2 z} - (m_3 + ik)\frac{n_3}{m_3^2}\mathrm{e}^{m_3 z}. \tag{24}$$

In view of Eqs. 38, Eq. 24 reduces to

$$\hat{b} = in_1 m_1 \mathrm{e}^{m_1 z} - in_2 m_2 \mathrm{e}^{m_2 z} - i\,\mathrm{sgn}(k) n_3 m_3 \mathrm{e}^{m_3 z}, \tag{25}$$

where $\mathrm{sgn}(k) = 1$ for $k > 0, -1$ for $k < 0$. Applying the impermeability and no-slip condition, in turn, in (23), yields

$$n_1 + n_2 + n_3 = 0, \tag{26}$$

$$n_1 m_1 + n_2 m_2 + n_3 m_3 = 0. \tag{27}$$

A third constraint on $n_1, n_2, and n_3$ is obtained from a boundary condition for the buoyancy. If the surface buoyancy $b(x, 0)$ is specified, then (25) yields

$$i\hat{b}_0 = -n_1 m_1 + n_2 m_2 + \mathrm{sgn}(k) n_3 m_3, \tag{28}$$

where $\hat{b}_0 \equiv \frac{1}{\sqrt{2\pi}} \int_{-\infty}^{\infty} \mathrm{e}^{-ikx} b(x, 0) \mathrm{d}x$. If the surface buoyancy flux is specified, then we evaluate $\partial/\partial z$ (Eq. 24) at $z = 0$, and simplify the resulting equation using (26), obtaining,

$$i\frac{\hat{Q}_0}{k} = \frac{n_1}{m_1} + \frac{n_2}{m_2} + \frac{n_3}{m_3}, \tag{29}$$

where $\hat{Q}_0 \equiv \frac{1}{\sqrt{2\pi}} \int_{-\infty}^{\infty} \mathrm{e}^{-ikx} \partial b(x, 0)/\partial z \mathrm{d}x$. The $b(x, 0)$ and $\partial b(x, 0)/\partial z$ functions are considered to vanish as $|x| \to \infty$ but are otherwise arbitrary. The solutions for $n_1, n_2,$ and n_3 in these two scenarios are provided in Appendix B.

We now consider the particular case of katabatic flow driven by a surface buoyancy or buoyancy flux that is proportional to the top-hat function

$$T_l(x) = \begin{cases} 1, & |x| < \frac{l}{2}, \\ 0, & \text{otherwise}, \end{cases} \tag{30}$$

where l is the non-dimensional forcing width. For the case of a top-hat buoyancy distribution $b(x, 0) = -T_l(x)$, the transformed surface buoyancy is

$$\hat{b}_0 = -\sqrt{\frac{2}{\pi}} \frac{\sin(kl/2)}{k}. \tag{31}$$

For a top-hat surface distribution of slope-normal buoyancy gradient $\partial b(x, 0)/\partial z = T_l(x)$ (positive gradient is associated with a negative buoyancy flux), the transformed slope-normal buoyancy gradient is

$$\hat{Q}_0 = \sqrt{\frac{2}{\pi}} \frac{\sin(kl/2)}{k}. \tag{32}$$

The solutions for ψ and b corresponding to these forcings are given in Appendices C and D.

4 Examples

In our evaluation of the top-hat solutions for l in the 0.5 to 40 range, the integrals in (51), (52), (66), and (67) were approximated numerically by summing the integrands over intervals $k \in [-1000, 0^-]$ and $k \in [0^+, 1000]$ with a spacing of $\Delta k = 0.002$, i.e., 10^6 waves are summed with the $k = 0$ point excluded to avoid a computational singularity. For larger l (up to 100), the range of k was reduced by a factor of 4 to meet the computational requirements of a larger physical domain. In both cases, the spectral resolution and range of k were deemed sufficient for an accurate evaluation of the solution. Reductions of range or resolution on the order of 25% produced almost imperceptible changes in the solutions over the domains of interest.

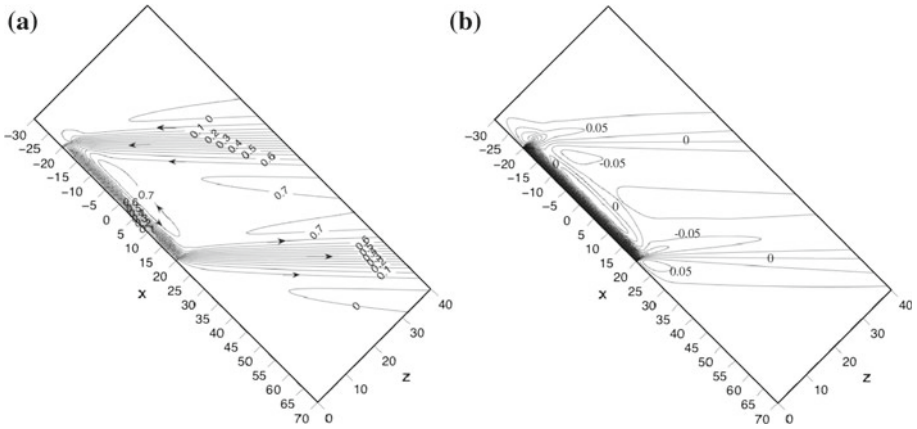

Fig. 5 Katabatic flow induced by a top-hat distribution of surface buoyancy of width $l = 40$. Contour plots of **a** streamfunction ψ and **b** buoyancy b are obtained from the Fourier analysis. Contour intervals for ψ and b are 0.05 and 0.025, respectively. All quantities are non-dimensional

Before examining these solutions, we consider some graphical implications of the non-dimensionalization (5) and (6). Recall that on a constant elevation surface, $Z = X \tan\alpha +$ const, while the equivalent non-dimensional relation is $z = x +$ const. Thus, on $x-z$ plots in which equal increments of plotting distance in the x and z directions correspond to equal increments in the values of x and z, lines of constant elevation cross the slope at 45° angles. Accordingly, if such plots are rotated by 45°, as in some of our figures, then a horizontal line represents constant elevation. This 45° graphical rotation property holds for all slope angles. We also note that for typical slope angles, the non-dimensionalization compresses the X axis relative to the Z axis. For α of 1° and 10°, the X to Z axis compression factors are ≈50 and ≈5, respectively. Thus, if one views an $x-z$ plot in which equal increments of plotting distance in the x and z directions correspond to equal increments in the values of x and z, and wants to envision a corresponding $X-Z$ plot in which the true aspect ratios of flow structures are represented, then one should stretch the $x-z$ plot in the x direction by a factor of $\cot\alpha$.

The streamfunction and buoyancy fields for a top-hat distribution of slope buoyancy of width $l = 40$ are shown in Fig. 5. The boundary-layer flow from $x \approx -10$ to $x \approx 15$ is characterized by a shallow katabatic jet of negatively buoyant fluid topped by a weak return flow of (slightly) positively buoyant fluid. As can be seen in Fig. 6, these features are in excellent agreement with the Prandtl solution. Thus, even though the flow as a whole is two-dimensional, the boundary-layer flow over the strip at sufficiently far distances from the strip edges becomes one-dimensional.

Also evident in Fig. 5a are two jets that penetrate far into the environment: an inward jet feeding into the katabatic jet near the upslope edge of the cold strip and an outward jet emanating from the katabatic boundary-layer flow into the environment near the downslope edge of the cold strip. These jets are nearly horizontal as they progress through the environment, but turn abruptly downward or upward as they enter or leave the katabatic boundary layer. The environmental jet speeds (not shown, but the speed can be inferred qualitatively from streamline spacing) decrease with horizontal distance from the slope along the jet axis and are substantially lower than the primary katabatic jet speed. The peak environmental jet speeds are only ≈30% of the peak katabatic jet speed. The environmental jet streamlines in Fig. 5a

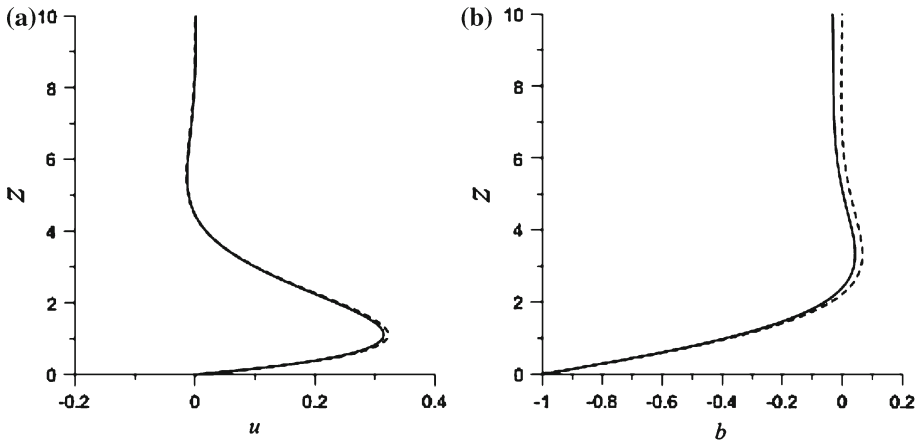

Fig. 6 Slope-normal profiles of **a** along-slope velocity component u and **b** buoyancy b near the centre of the cold strip ($x = 0$) for katabatic flow driven by a top-hat distribution of surface buoyancy of width $l = 40$, the case considered in Fig. 5. *Solid lines* depict the solution from the Fourier analysis. *Dashed lines* depict the corresponding Prandtl solution. All quantities are non-dimensional

are visually similar to the streamlines in the flow of a viscous stably stratified fluid toward a line sink (cf. Fig. 3 of Koh 1966). Koh's numerical and experimental analyses showed that the viscous line sink flow satisfies a self-similarity principle in which the height of any given streamline above the jet axis increases as the 1/3 power of distance from the sink. By means of measurements of the thickness of our inward jet at three vertical cross sections along the jet axis, we conclude that our inward jet is also well described by the same similarity model. The thicknesses may be obtained subjectively by measuring the distance between upper and lower streamlines on either side of the jet on a blown-up version of Fig. 5a. Measurements at two of the cross sections are used to fix the origin of a virtual sink and fix the proportionality constant in the 1/3 power law. The measured thickness of the jet at a third cross section was found to be in good agreement with the power-law-predicted thickness.

The thermal structure of the environmental jets plays a crucial role in the vorticity dynamics that makes those jets dynamically feasible. Because the inward jet entrains environmental air of known characteristics, and the outward jet, however, is an extension of the katabatic jet, we restrict our attention to the more straightforward analysis of the inward jet. Although this jet has a pronounced horizontal velocity component, the streamlines in the upper flank of the jet have a slight concave-down curvature, while the streamlines in the lower flank of the jet have a slight concave-up curvature. Warming due to subsidence along the downward curving streamlines results in small positive buoyancy values in the upper flank (Fig. 5b). The largest values of b are located where the streamlines are curved the most, which is near the top of the katabatic boundary layer. Accordingly, in the upper flank $-\partial b/\partial x^* > 0$, and there is baroclinic generation of positive (into page) Y-component of vorticity. Similarly, in the lower flank, differential ascent in the presence of the ambient stable stratification yields $-\partial b/\partial x^* < 0$, and there is generation of negative Y-component of vorticity. These baroclinically generated vorticity patterns permit the flow to be jet-like, i.e., to be nearly unidirectional along a central jet axis, and decrease in strength above (into-page vorticity) and below (out-of-page vorticity) the central axis.

Another interesting feature is a small rotor-like feature (vortex) that straddles the upslope edge of the strip. This vortex is barely discernable in Fig. 5a, but can be seen in the close-up

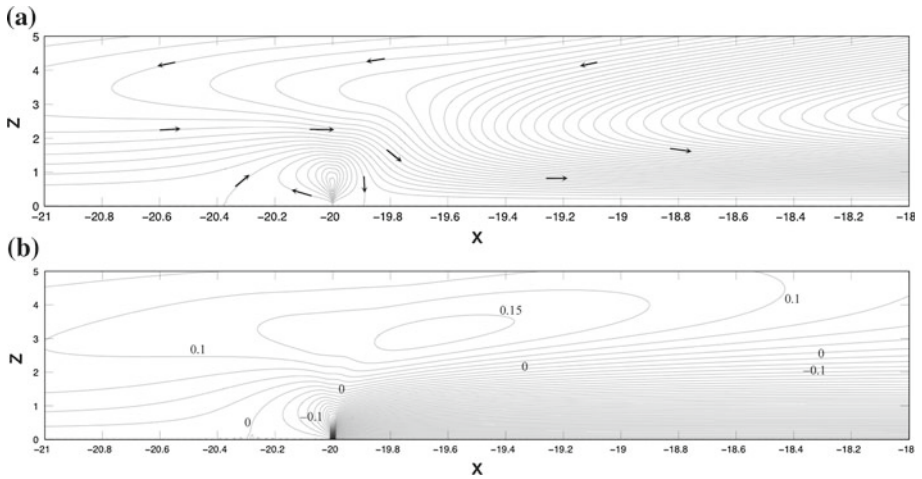

Fig. 7 Close-up view of **a** streamfunction ψ and **b** buoyancy b in the vicinity of the upslope edge of the cold strip ($x = -20$) for the case shown in Fig. 5. A rotor-like feature in ψ appears in the baroclinic zone in the immediate vicinity of this upslope edge. Contour intervals for ψ and b are 0.01 and 0.025, respectively. All quantities are non-dimensional

view of Fig. 7a that has also been stretched to give the reader a true aspect ratio perspective for the case of a small slope angle. Not surprisingly, the vortex is located within a zone of a strong baroclinicity (Fig. 7b). The large horizontal buoyancy gradient near the upslope edge of the cold strip produces the positive Y component vorticity characterizing the vortex. One can also see in Fig. 7b a small elevated blob of negative buoyancy slightly upslope from the strip edge. This negative buoyancy arises from the adiabatic cooling of the air parcels in the rising branch of the upslope vortex.

In contrast, no vortex is found in the baroclinic zone on the downslope edge. Instead, the positive horizontal buoyancy gradient near that edge produces the negative (out-of-page) curvature vorticity that allows the katabatic jet to turn into the environment where it emerges as the outward environmental jet. The transition of the inward environmental jet into the katabatic jet near the upslope edge is more circuitous.

Also evident in Figs. 5b and 7b is a belt of warm air roughly centered above the upslope edge of the cold strip at $z \approx 3$. The peak value of the buoyancy in this warm belt is about 15% of the magnitude of the slope buoyancy, which is unity. The warm belt arises from subsidence warming where the inward environmental jet turns (descends) into the katabatic jet.

Thermal belts of warm air analogous to those found in our study have long been observed along slopes in hilly or mountainous terrain. Thermal belts have been documented in North Carolina, U.S.A. (Cox 1920; Dunbar 1966), New Zealand (Sturman et al. 1999), Japan (Yoshino 1984; Kobayashi et al. 1994; Tanaka et al. 1998; Ueda et al. 2003), and other locations worldwide. These belts are often found during clear and calm nights in association with cold air drainage flows, and the mechanism producing the warming usually attributed to subsidence warming or to horizontal streaming of a warm counter flow toward the slope in response to cold air drainage at lower levels (e.g., Yoshino 1984). Thus, the thermal belts in our study likely share a key mechanism with some of the observed thermal belts, namely, the changing characteristics of flow down the slope, induces the flow of warmer or potentially warmer environmental air toward the slope. On the other hand, since the belts in the above studies formed over terrain with significant changes in slope angle, and the belts in our study,

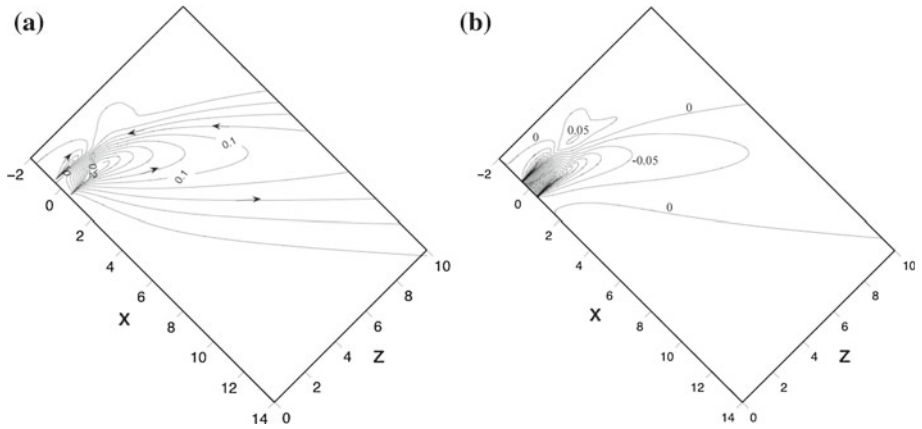

Fig. 8 Katabatic flow induced by a top-hat distribution of surface buoyancy of width $l = 1$. Contour plots of **a** streamfunction ψ and **b** buoyancy b obtained from the Fourier analysis. Contour intervals for ψ and b are 0.02 and 0.025, respectively. All quantities are non-dimensional

however, arose from an inhomogeneous buoyancy forcing on a uniform slope, the underlying forcing mechanisms are different. We suggest that the mechanism of thermal belt formation in our study is one of several possible modes that might be found in nature, a plausible one in cases where a downslope acceleration of katabatic flow is caused by inhomogeneous buoyancy forcing.

Solutions for other strip widths l in a 10–100 range (not shown) displayed the same structures—Prandtl-like katabatic jet, inward and outward environmental jets, upslope vortex, and thermal belt—as found in the $l = 40$ case. Moreover, these structures were in very close quantitative agreement with each other across this range of l. In other words, for large l, the main flow features became independent of l. In this large-l regime, the length, velocity, and buoyancy scales in (6) are not merely formal non-dimensionalization factors, but are the actual scales characterizing the length, velocity, and buoyancy of flow structures (apart from constants of proportionality).

The constants of proportionality can be obtained by examining flow structures in any of the large-l solutions. For instance, a dimensional height scale for the upslope vortex, defined as, say, the distance of the stagnation point inside the vortex above the slope, is of the form $h_{\mathrm{vort}} = c_{\mathrm{vort}} Z_{\mathrm{s}}$, where c_{vort} is the non-dimensional height of the vortex. From Fig. 7a, we see that $c_{\mathrm{vort}} \approx 0.8$, and we obtain a large-$l$ relation $h_{\mathrm{vort}} = 0.8(\nu\kappa)^{1/4}(N \sin\alpha)^{-1/2}$. Similarly, we find the height of the peak buoyancy in the warm belt is $h_{\mathrm{belt}} = c_{\mathrm{belt}} Z_{\mathrm{s}}$, where $c_{\mathrm{belt}} \approx 3$. The main differences in the large-l solutions are in the spacing between the environmental jets and in the along-slope extent of the Prandtl-like jet, both of which, not surprisingly, increase with l. A strip width of $l = 10$ is the approximate lower bound of l for the full development of a Prandtl flow regime.

The streamfunction and buoyancy fields for l in the range from 0.5 to 5 can be broadly represented by the $l = 1$ case (Fig. 8). In these smaller l cases, the primary katabatic jet does not fully develop into a Prandtl jet, and it is weaker than in the large l cases. Environmental jets do form, but they no longer penetrate far into the environment. Instead, the jets merge above the slope, with merger occurring progressively closer to the slope as l decreases. The circulation associated with these jets is also more vortex-like than before. Indeed, at some point in the succession of decreasing l, what we perceive to be counter-directed environ-

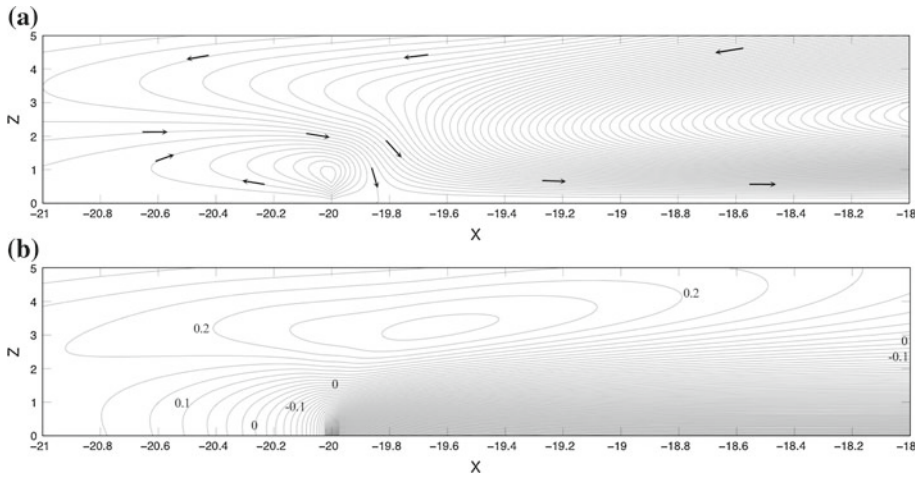

Fig. 9 Close-up view of **a** streamfunction ψ and **b** buoyancy b obtained from the Fourier analysis in the vicinity of the upslope edge of the cold strip ($x = -20$) for katabatic flow induced by a top-hat distribution of surface buoyancy flux of width $l = 40$. Contour intervals for ψ and b are 0.01 and 0.025, respectively. Peak slope buoyancy is ≈ -1.6. All quantities are non-dimensional

mental jets is perceived as a large vortex. However, on the upslope edge of the strip, a small vortex is still found, as in the large l solutions.

We also considered local katabatic flows induced by top-hat distributions of surface buoyancy flux. The primary katabatic jets, large-l Prandtl regimes, counter-flowing environmental jets, vortices, and thermal belts with peak buoyancy $\approx$15% of the peak magnitude of the surface buoyancy were all present in these flows and strongly resembled those for the flows driven by a top-hat surface buoyancy disturbance. The most significant difference appeared to be a wider and weaker upslope vortex and associated baroclinic zone in the flux-forcing case. The larger lateral extension of the zone of negative buoyancy near the strip edge in that case was due to the zero-buoyancy-flux boundary condition outside of the strip. This permitted the negative buoyancy arising from adiabatic cooling in the ascending branch of the vortex to diffuse down to the surface. Such surface cooling is precluded by a zero-buoyancy boundary condition. A close-up view of the vortex and baroclinic zone for $l = 40$ is presented in Fig. 9 (cf. Fig. 7). The corresponding plots of u (not shown) indicate that the ratio of peak u in the upslope vortex to peak u in the primary katabatic jet decreases from $\approx$0.5 in the buoyancy-forced case to $\approx$0.3 in the flux-forced case.

5 Numerical Solution of the Nonlinear Problem

The nonlinear governing equations were solved numerically for the initial value problem in which a top-hat surface buoyancy forcing was suddenly imposed at $t = 0$, and thereafter maintained. These solutions were used to verify the analytic results for a weak thermal disturbance, elucidate the nonlinear aspects of the flow driven by a strong thermal disturbance, and examine the transient development of the flow leading to the steady state. The governing parameters were chosen to correspond to the flow over a strip with non-dimensional width of $l \approx 40$, a case considered in Sect. 4.

The numerical procedures used herein are patterned on the studies of Fedorovich et al. (2001) and were previously employed in the natural convection and katabatic studies of Shapiro and Fedorovich (2004b, 2006, 2008), Fedorovich and Shapiro (2009a,b), and Burkholder et al. (2009). The numerically solved equations are the Boussinesq equations of motion, thermal energy, and mass conservation without boundary-layer or hydrostatic approximations, together with the standard elliptic equation for the perturbation pressure that results from taking the divergence of the equations of motion. Although the code is generally capable of simulating three-dimensional phenomena, it was used here in an effectively two-dimensional mode by allocating only four grid cells in the cross-slope direction. The model equations are discretized on a staggered, slope-following Cartesian grid with a uniform spacing in a rectangular domain. The spatial derivatives are discretized with second-order finite difference expressions, and the prognostic variables are integrated using a leapfrog scheme with weak Asselin filter. The elliptic equation for the perturbation pressure is solved at each timestep with a fast-Fourier transform technique over planes tangent to the slope, and using a tri-diagonal matrix inversion in the slope-normal direction. On the slope, no-slip and impermeability conditions are imposed on the velocity components, the surface buoyancy is prescribed, and the slope-normal derivative of the perturbation pressure is calculated as a residual from the slope-normal equation of motion. At the top of the computational domain, the normal gradients of all variables are set to zero. Periodic boundary conditions are imposed for all variables on the four lateral boundaries.

Because of the stringent computational grid requirements described below, it was preferable to implement a parallel version of the code. The model domain was decomposed into 256 equal-sized volumes partitioned in the along-slope direction. The slope-normal and cross-slope dimensions of each sub-domain were equal to those of the original domain. Each sub-domain was assigned a processor to perform the numerical calculations, and inter-processor communication was handled through the message–passage interface subroutine calls.

The physical parameters in our numerical experiments were set to $\alpha = 15°$, $N = 0.01\,\mathrm{s}^{-1}$, $\nu = \kappa = 1\,\mathrm{m}^2\,\mathrm{s}^{-1}$, and $L = 2.8\,\mathrm{km}$ ($l \approx 40$). Preliminary tests (not shown) were made to determine appropriate grid spacing and computational domain dimensions. We sought a grid spacing that would resolve the primary katabatic jet and a computational domain that would allow a (nearly) steady state to be realized at low levels over several tens of Prandtl boundary-layer depths before artifacts arising from the upper and lateral boundaries began to contaminate the solution. A grid spacing of $\Delta X = \Delta Z = 2\,\mathrm{m}$, domain height of $H \approx 8.1\,\mathrm{km}$ and domain width of $D \approx 32.7\,\mathrm{km}$ allowed us to satisfy these competing resolution and size requirements, and was at the edge of our computational resources. The domain sizes considered here are substantially larger than those adopted in Burkholder et al. (2009).

Next, a quasi-linear flow regime was simulated numerically by imposing a small (1 K) perturbation of the strip temperature. Gravity waves arose in the flow from the applied abrupt thermal forcing, and the largest amplitude waves appeared to be generated near the downslope edge of the strip, where the primary katabatic jet decelerated. As these waves propagated away from the slope, an expanding steady-state flow structure was left behind. The steady-state solution (not shown) was compared with the purely linear boundary-layer solution described in Sect. 4. All the features in the purely linear boundary-layer solution (katabatic jet, counter-flowing environmental jets, upslope vortex, and thermal belt) were obtained in the numerical solution and both solutions were generally in close agreement. The largest differences were in the intensity of the thermal belt and vortex, both of which were slightly (≈20%) weaker in the numerical simulation. That the largest differences were near a strip edge is not surprising since the numerical model includes along-slope derivatives in the stress and diffusion terms that were neglected in the boundary-layer theory.

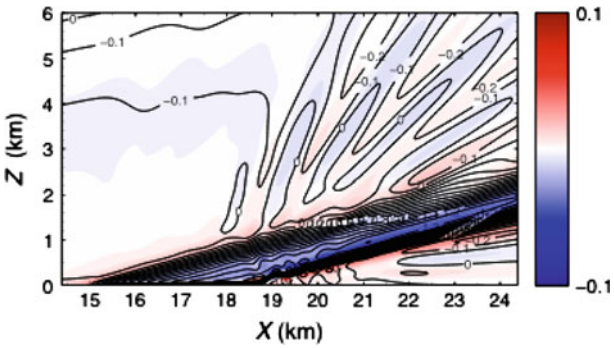

Fig. 10 Numerical solution for a flow induced by a top-hat distribution of surface buoyancy at $t = 81$ min. The large vertical extent of the plot highlights the environmental jets and gravity waves (at the expense of the shallow katabatic jet). Non-dimensional buoyancy is shaded in *blue* and *red*. Streamfunction (normalized) is contoured with *solid lines*. The slope temperature perturbation is 3 K. Other parameters are $\alpha = 15°$, $N = 0.01\,\mathrm{s}^{-1}$, $\nu = \kappa = 1\,\mathrm{m}^2\,\mathrm{s}^{-1}$, and the strip width is $L = 2.8$ km ($l \approx 40$). The cold strip extends approximately from $X = 15$ km to $X = 17.8$ km. Only a portion of the computational domain is depicted

Non-linear effects grew in importance in experiments with progressively larger slope thermal perturbations, and the model became numerically unstable for a slope temperature perturbation of 5 K. The instability appears to have arisen from convective overturning in gravity waves emanating from the downslope edge of the strip. The development of turbulence in regions of breaking internal waves, even over two-dimensional obstacles, is a fundamentally three-dimensional process (Yakovenko et al. 2011).

In the remainder of this section, we focus on results of simulation with a slope temperature perturbation of 3 K, an experiment in which nonlinear effects could be clearly identified in an extensive steady-state wake. A large-scale overview of the buoyancy and streamfunction fields for this case at $t = 81$ min is presented in Fig. 10, and a close-up view of those fields and the U and W fields is presented in Fig. 11. At the considered time, a steady state had been attained at low levels, roughly for $z < 300$ m, but transient waves were still propagating at middle and upper levels. Although the gross features of the primary katabatic jet and environmental jets at this time are similar to those in the linear solution, there are some notable differences. First, because of the advection terms, the primary katabatic jet extends further downslope from the strip than it does in the linear case. The layer of strongly negatively buoyant air extends ≈0.5 km down the slope, while the jet of high momentum air extends nearly 1 km down the slope. That the layer of negative buoyancy does not extend as far down the slope as the high-momentum air (the jet actually becomes positively buoyant for ≈0.5 km before turning away from the slope) can be attributed to warming of the jet due to subsidence. Since the katabatic jet has overshot its equilibrium level by the time it turns away from the slope, the mechanism is present for this jet to have gravity-wave-like characteristics as it exits into the environment. Note the pronounced serpentine structure of the velocity and streamfunction in the lowest ≈300 m of the outward environmental jet. Results from other times indicate that this serpentine structure, like the other low-level structures, is nearly in a steady state. A pronounced gravity-wave signature attending decelerating katabatic flow was a key feature of the inhomogeneously forced flows in Shapiro and Fedorovich (2007).

As in the linear solution, the horizontal jets in the nonlinear solution expand gradually with distance from the slope and penetrate deeply into the environment, with warm air overlying cold air in the inward jet, and an opposite thermal arrangement in the outward jet (Figs. 10, 11). However, in contrast to the symmetric arrangement in the linear solution,

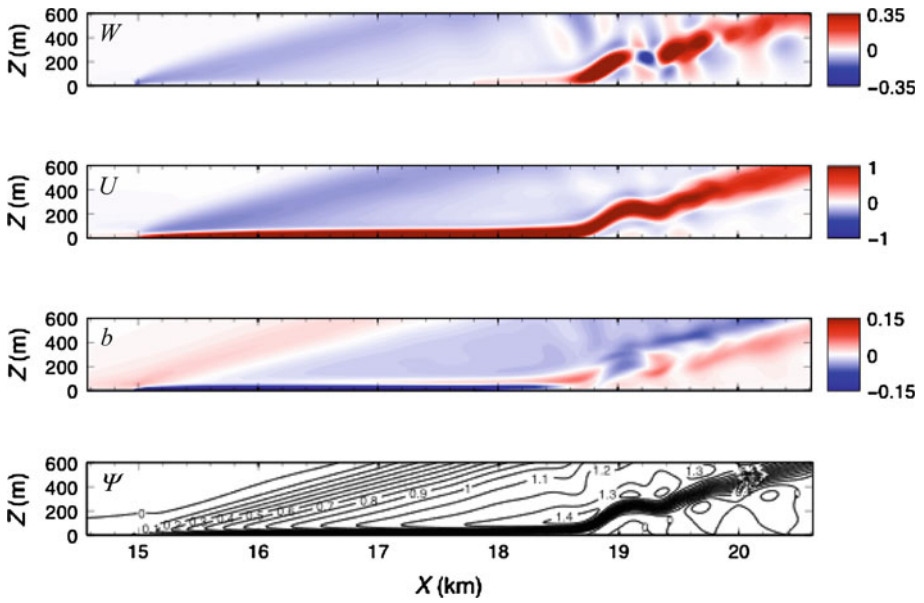

Fig. 11 Close up view of U and W ($\mathrm{m\,s^{-1}}$), b, and ψ (normalized) for the flow case illustrated in Fig. 10. The cold strip extends approximately from $X = 15\,\mathrm{km}$ to $X = 17.8\,\mathrm{km}$. The *colour bars* are chosen to highlight structures above the primary katabatic jet. Values exceeding the limits in the *colour bars* are present in and near the primary katabatic jet

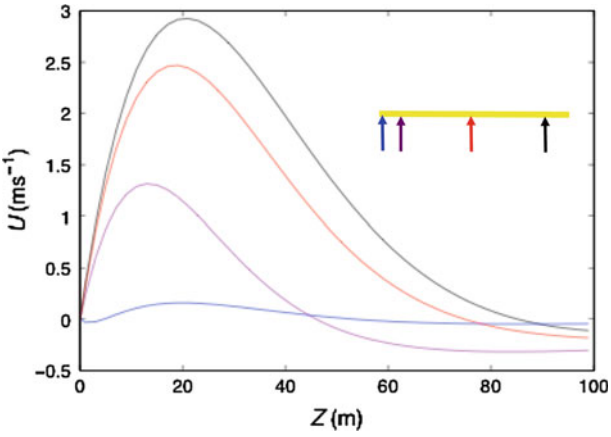

Fig. 12 Down-slope velocity component U as a function of Z in the primary katabatic jet at four locations along the cold strip (*yellow bar* in *inset*) for the flow case shown in Fig. 10: *blue*—at upslope edge of strip; *violet*—at distance $L/8$ downstream from upslope edge of strip; *red* at centre of strip; and *black* at distance $L/8$ upstream from downslope edge of strip

the inward environmental jet in the numerical solution is wider and weaker than the outward environmental jet. The widened inward jet is associated with a widened zone of entrainment of environmental air into the primary katabatic jet. Accordingly, the Prandtl-jet (boundary-layer) regime for U is delayed down the slope. Slope-normal profiles of U and b at four locations along the cold strip are shown in Figs. 12 and 13, respectively. Within a downslope

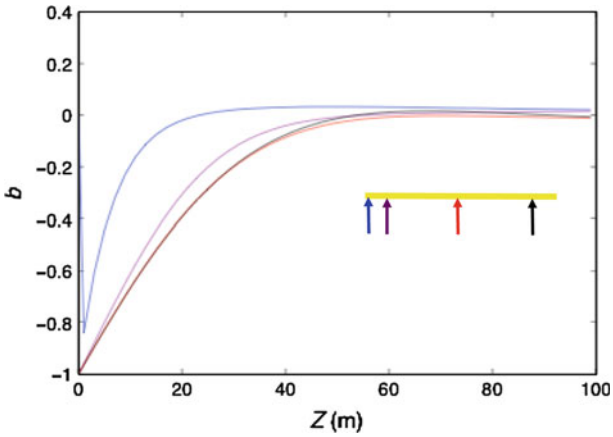

Fig. 13 Non-dimensional buoyancy b as a function of Z in the primary katabatic jet at four locations along the cold strip (*yellow bar* in *inset*) for the flow case shown in Fig. 10. The locations are identified in Fig. 12

distance of $L/8$ from the upslope edge of the strip (violet curve), the b profile is in good agreement with the Prandtl solution. In contrast, the U profile develops more gradually down the slope and is still only ≈75% of the value of the peak U ($3.22\,\mathrm{m\,s^{-1}}$) in the Prandtl solution at the half-width location. At a distance $L/8$ upslope from the lower edge of the strip, the height of the jet maximum differs imperceptibly from the height obtained from the Prandtl solution (≈21.8 m), and the peak U now differs from the Prandtl value by less than 10%.

Finally, we note that although there was an upslope vortex present in this numerical simulation (not shown), its lower branch (upslope flow) was very weak and possibly not adequately resolved. A shallow ($Z < 6\,\mathrm{m}$) zone of weak upslope vortex flow is evident in the U profile on the upslope edge of the strip (blue curve of Fig. 12).

6 Summary

The two-dimensional flow of a stably stratified fluid down an inhomogeneously cooled planar slope was studied within a linearized boundary-layer framework. The slope angle, Brunt–Väisälä frequency, and coefficients of eddy viscosity and diffusivity were treated as constants. Non-dimensional variables were introduced to clear the problem of as many parameters as possible. For flows induced by a top-hat profile of surface buoyancy or buoyancy flux, the problem was controlled by a single parameter—the non-dimensional cold strip width l. For large l, the flow variables became independent of l, i.e., they became universal functions of the non-dimensional variables. Key flow structures revealed through the linear solution were

- a primary katabatic jet that became the one-dimensional Prandtl jet for sufficiently wide strips,
- counter-directed (inward and outward) horizontal environmental jets that entered and left the katabatic boundary-layer region, and penetrated deeply into the environment,
- a low-level vortex that straddled the baroclinic zone on the upslope edge of the strip, and
- a warm thermal belt that overlaid the boundary layer above the upslope edge of the strip.

Numerical simulations of the corresponding nonlinear problem were used to verify the analytic study, elucidate the nonlinear aspects of the flow, and examine the transient development

of the flow leading to the steady state. The main features in the linear solution were also found in the nonlinear solution but with some notable differences:

- the development of a Prandtl regime was delayed down the strip;
- buoyancy and momentum advection became noticeable downslope of the strip;
- the outward jet was narrower and more intense than the inward jet; and
- the outward jet, which arose from the primary katabatic jet after it had overshot its equilibrium level, had a pronounced serpentine structure as it intruded into the environment.

The two-dimensional laminar problem considered in this article was investigated as a prelude to more realistic numerical studies of turbulent katabatic flows.

Acknowledgments The authors thank Petra Klein and Sean Arms for helpful discussions about this study. This research was supported in part by the United States National Science Foundation through Grant ATM-0622745. A part of the computing was performed at the University of Oklahoma Supercomputing Center for Education & Research (OSCER). The authors thank OSCER Director Henry Neeman for allocating the computing time needed to develop and test the parallel version of the numerical model used in this study. The detailed comments of one of the anonymous reviewers are gratefully acknowledged.

Appendix A: Solution of Cubic Equation 22

Although analytic formulae (Cardano formulae) are available for the solutions of cubic equations, the one-third roots appearing in those formulae have multiple branches, some of which do not lead to solutions (Jeffrey and Norman 2004). Thus, in practice, use of the explicit formulae might require that all of the candidate solutions be verified. Fortunately, (22) can be readily solved implicitly, thus bypassing the need to evaluate many candidate solutions.

In an explicit approach, one can think of the solutions m_j of (22) as functions of k having the polar form $m_j(k) = R_j(k)\mathrm{e}^{i\phi_j(k)}$, where R_j and ϕ_j are k-dependent amplitude and phase functions, respectively. In contrast, in an implicit (parametric) approach, one may treat k as a set of functions $k_j(\phi)$ of the phase parameter ϕ, and work with m_j in the polar form:

$$m_j(\phi) = R_j(\phi)\mathrm{e}^{i\phi}, \tag{33a}$$

$$k_j = k_j(\phi). \tag{33b}$$

To restrict attention to m_j with negative real part, one need only consider ϕ in the range $\pi/2 < \phi < 3\pi/2$.

We consider (22) in the form:

$$m_j^3 = s_j\left(im_j - k_j\right), \tag{34}$$

where $s_j = 1$ or -1. Applying (33a) and (33b) in (34), and taking real and imaginary parts yields

$$R_j^3 \cos 3\phi + s_j R_j \sin\phi + s_j k_j = 0, \tag{35}$$

$$R_j^3 \sin 3\phi - s_j R_j \cos\phi = 0, \tag{36}$$

from which follows the parametric solution:

$$k_j(\phi) = -R_j(\phi)\frac{\cos 2\phi}{\sin 3\phi}, \tag{37a}$$

$$R_j(\phi) = \sqrt{s_j \frac{\cos\phi}{\sin 3\phi}}. \tag{37b}$$

Setting s_j to 1 and -1, in turn, (37a) and (37b) yields the implicit solutions shown in Fig. 3. We adopt the following ordering convention: (i) the $j = 1$ solution corresponds to $s_1(\phi) = 1$; (ii) the $j = 2$ solution corresponds to $s_2(\phi) = -1$; and (iii) the $j = 3$ solution corresponds to $s_3(\phi) = 1$ for $\pi/2 < \phi < 2\pi/3$ ($90° < \phi < 120°$), and $s_3(\phi) = -1$ for $4\pi/3 < \phi < 3\pi/2$ ($240° < \phi < 270°$). From the behaviour of the $k_3(\phi)$ curves in Fig. 3, we see that the $j = 3$ solution corresponds to $s_3(\phi) = 1$ for $k_3 < 0$, and to $s_3(\phi) = -1$ for $k_3 > 0$.

The explicit solutions for m_j can be obtained from the implicit solutions by treating k as the independent variable and interpolating the implicit solutions to a grid of equally spaced points along the k axis. The real and imaginary parts of these solutions are shown in Fig. 4.

For the analysis of the $\hat{b}$ variable, it will be convenient to work with (34) rewritten separately for $j = 1, 2$ and 3 as

$$\frac{m_1 + ik}{m_1^2} = -im_1, \tag{38a}$$

$$\frac{m_2 + ik}{m_2^2} = im_2, \tag{38b}$$

$$\frac{m_3 + ik}{m_3^2} = \begin{cases} im_3, & k > 0, \\ -im_3, & k < 0. \end{cases} \tag{38c}$$

Appendix B: Solution for n_1, n_2, and n_3

In the case where the slope buoyancy is specified, the constants $n_1, n_2,$ and n_3 satisfy the three linear algebraic equations (26)–(28). These equations are solved as

$$n_1 = \begin{cases} -\dfrac{i\hat{b}_0}{2m_1}, & k > 0, \\ -\dfrac{i\hat{b}_0}{2m_2}\dfrac{(m_3 - m_2)}{(m_3 - m_1)}, & k < 0, \end{cases} \tag{39}$$

$$n_2 = \begin{cases} \dfrac{i\hat{b}_0}{2m_1}\dfrac{(m_3 - m_1)}{(m_3 - m_2)}, & k > 0, \\ \dfrac{i\hat{b}_0}{2m_2}, & k < 0, \end{cases} \tag{40}$$

$$n_3 = \begin{cases} \dfrac{i\hat{b}_0}{2m_1}\dfrac{(m_1 - m_2)}{(m_3 - m_2)}, & k > 0, \\ \dfrac{i\hat{b}_0}{2m_2}\dfrac{(m_1 - m_2)}{(m_3 - m_1)}, & k < 0. \end{cases} \tag{41}$$

After rationalizing the denominators in (39)–(41), and using the polar form $m_j = R_j \exp(i\phi_j)$ introduced in Appendix A, we obtain

$$n_1 = \begin{cases} -\dfrac{i\hat{b}_0}{2R_1}\mathrm{e}^{-i\phi_1}, & k > 0, \\ -\dfrac{i\hat{b}_0}{2R_2}\dfrac{R_3^2\mathrm{e}^{-i\phi_2} - R_1R_3\mathrm{e}^{-i(\phi_1+\phi_2-\phi_3)} - R_2R_3\mathrm{e}^{-i\phi_3} + R_1R_2\mathrm{e}^{-i\phi_1}}{R_1^2 + R_3^2 - 2R_1R_3\cos(\phi_1 - \phi_3)}, & k < 0, \end{cases} \tag{42}$$

$$n_2 = \begin{cases} \dfrac{i\hat{b}_0}{2R_1} \dfrac{R_3^2 e^{-i\phi_1} - R_2 R_3 e^{-i(\phi_1+\phi_2-\phi_3)} - R_1 R_3 e^{-i\phi_3} + R_1 R_2 e^{-i\phi_2}}{R_2^2 + R_3^2 - 2R_2 R_3 \cos(\phi_2 - \phi_3)}, & k > 0, \\ \dfrac{i\hat{b}_0}{2R_2} e^{-i\phi_2}, & k < 0, \end{cases} \tag{43}$$

$$n_3 = \begin{cases} \dfrac{i\hat{b}_0}{2R_1} \dfrac{R_2^2 e^{-i\phi_1} - R_2 R_3 e^{-i(\phi_1-\phi_2+\phi_3)} + R_1 R_3 e^{-i\phi_3} - R_1 R_2 e^{-i\phi_2}}{R_2^2 + R_3^2 - 2R_2 R_3 \cos(\phi_2 - \phi_3)}, & k > 0, \\ -\dfrac{i\hat{b}_0}{2R_2} \dfrac{R_1^2 e^{-i\phi_2} - R_1 R_3 e^{-i(-\phi_1+\phi_2+\phi_3)} + R_2 R_3 e^{-i\phi_3} - R_1 R_2 e^{-i\phi_1}}{R_1^2 + R_3^2 - 2R_1 R_3 \cos(\phi_1 - \phi_3)}, & k < 0. \end{cases} \tag{44}$$

In the case where the buoyancy flux is specified, n_1, n_2, and n_3 satisfy (26), (27), and (29). These equations are solved as

$$n_1 = \frac{i\hat{Q}_0}{k} \frac{m_1 m_2 m_3}{(m_3 - m_1)(m_2 - m_1)}, \tag{45}$$

$$n_2 = -\frac{i\hat{Q}_0}{k} \frac{m_1 m_2 m_3}{(m_3 - m_2)(m_2 - m_1)}, \tag{46}$$

$$n_3 = \frac{i\hat{Q}_0}{k} \frac{m_1 m_2 m_3}{(m_3 - m_1)(m_3 - m_2)}, \tag{47}$$

or, after rationalizing the denominators,

$$n_1 = \frac{i\hat{Q}_0 R_1 R_2 R_3}{k} \frac{R_2 R_3 e^{i\phi_1} - R_1 R_3 e^{i\phi_2} - R_1 R_2 e^{i\phi_3} + R_1^2 e^{i(-\phi_1+\phi_2+\phi_3)}}{\left[R_1^2 + R_3^2 - 2R_1 R_3 \cos(\phi_1 - \phi_3)\right]\left[R_1^2 + R_2^2 - 2R_1 R_2 \cos(\phi_1 - \phi_2)\right]}, \tag{48}$$

$$n_2 = \frac{i\hat{Q}_0 R_1 R_2 R_3}{k} \frac{R_1 R_3 e^{i\phi_2} - R_2 R_3 e^{i\phi_1} - R_1 R_2 e^{i\phi_3} + R_2^2 e^{i(\phi_1-\phi_2+\phi_3)}}{\left[R_2^2 + R_3^2 - 2R_2 R_3 \cos(\phi_2 - \phi_3)\right]\left[R_1^2 + R_2^2 - 2R_1 R_2 \cos(\phi_1 - \phi_2)\right]}, \tag{49}$$

$$n_3 = \frac{i\hat{Q}_0 R_1 R_2 R_3}{k} \frac{R_3^2 e^{i(\phi_1+\phi_2-\phi_3)} - R_2 R_3 e^{i\phi_1} - R_1 R_3 e^{i\phi_2} + R_1 R_2 e^{i\phi_3}}{\left[R_1^2 + R_3^2 - 2R_1 R_3 \cos(\phi_1 - \phi_3)\right]\left[R_2^2 + R_3^2 - 2R_2 R_3 \cos(\phi_2 - \phi_3)\right]}. \tag{50}$$

Appendix C: Solution for Flow Driven by a Top-Hat Surface Buoyancy

For the case of a top-hat surface buoyancy distribution, the transformed slope buoyancy is given by (31). Applying (42)–(44) and (31) in (23) and (25), and taking the inverse transforms, yields the solution for ψ and b as

$$\psi = -\int_0^\infty \frac{\sin(kl/2)}{2\pi k R_1} \sum_{j=1}^{3} e^{zR_j \cos\phi_j} A_j^+ \, dk - \int_{-\infty}^0 \frac{\sin(kl/2)}{2\pi k R_2} \sum_{j=1}^{3} e^{zR_j \cos\phi_j} A_j^- \, dk, \tag{51}$$

$$b = -\int_0^\infty \frac{\sin(kl/2)}{2\pi k R_1} \sum_{j=1}^{3} e^{zR_j \cos\phi_j} R_j B_j^+ \, dk - \int_{-\infty}^0 \frac{\sin(kl/2)}{2\pi k R_2} \sum_{j=1}^{3} e^{zR_j \cos\phi_j} R_j B_j^- \, dk, \tag{52}$$

where A_j^+, A_j^-, B_j^+, and B_j^- $(j = 1, 2, 3)$ are planar wave functions of the argument

$$\chi_j \equiv kx + zR_j \sin\phi_j. \tag{53}$$

These wave functions are obtained as

$$A_1^+ \equiv \sin(\chi_1 - \phi_1), \tag{54}$$

$$A_2^+ \equiv \frac{-R_3^2 \sin(\chi_2-\phi_1)+R_2R_3 \sin(\chi_2-\phi_1-\phi_2+\phi_3)+R_1R_3 \sin(\chi_2-\phi_3)-R_1R_2 \sin(\chi_2-\phi_2)}{R_2^2+R_3^2-2R_2R_3 \cos(\phi_2-\phi_3)}, \tag{55}$$

$$A_3^+ \equiv \frac{-R_2^2 \sin(\chi_3-\phi_1)+R_2R_3 \sin(\chi_3-\phi_1+\phi_2-\phi_3)-R_1R_3 \sin(\chi_3-\phi_3)+R_1R_2 \sin(\chi_3-\phi_2)}{R_2^2+R_3^2-2R_2R_3 \cos(\phi_2-\phi_3)}, \tag{56}$$

$$A_1^- \equiv \frac{R_3^2 \sin(\chi_1-\phi_2)-R_1R_3 \sin(\chi_1-\phi_1-\phi_2+\phi_3)-R_2R_3 \sin(\chi_1-\phi_3)+R_1R_2 \sin(\chi_1-\phi_1)}{R_1^2+R_3^2-2R_1R_3 \cos(\phi_1-\phi_3)}, \tag{57}$$

$$A_2^- \equiv -\sin(\chi_2 - \phi_2), \tag{58}$$

$$A_3^- \equiv \frac{R_1^2 \sin(\chi_3-\phi_2)-R_1R_3 \sin(\chi_3+\phi_1-\phi_2-\phi_3)+R_2R_3 \sin(\chi_3-\phi_3)-R_1R_2 \sin(\chi_3-\phi_1)}{R_1^2+R_3^2-2R_1R_3 \cos(\phi_1-\phi_3)}, \tag{59}$$

$$B_1^+ \equiv \cos\chi_1, \tag{60}$$

$$B_2^+ \equiv \frac{R_3^2 \cos(\chi_2+\phi_2-\phi_1)-R_2R_3 \cos(\chi_2-\phi_1+\phi_3)-R_1R_3 \cos(\chi_2+\phi_2-\phi_3)+R_1R_2 \cos\chi_2}{R_2^2+R_3^2-2R_2R_3 \cos(\phi_2-\phi_3)}, \tag{61}$$

$$B_3^+ \equiv \frac{R_2^2 \cos(\chi_3-\phi_1+\phi_3)-R_2R_3 \cos(\chi_3-\phi_1+\phi_2)+R_1R_3 \cos\chi_3-R_1R_2 \cos(\chi_3-\phi_2+\phi_3)}{R_2^2+R_3^2-2R_2R_3 \cos(\phi_2-\phi_3)}, \tag{62}$$

$$B_1^- \equiv \frac{R_3^2 \cos(\chi_1+\phi_1-\phi_2)-R_1R_3 \cos(\chi_1-\phi_2+\phi_3)-R_2R_3 \cos(\chi_1+\phi_1-\phi_3)+R_1R_2 \cos\chi_1}{R_1^2+R_3^2-2R_1R_3 \cos(\phi_1-\phi_3)}, \tag{63}$$

$$B_2^- \equiv \cos\chi_2, \tag{64}$$

$$B_3^- \equiv \frac{R_1^2 \cos(\chi_3-\phi_2+\phi_3)-R_1R_3 \cos(\chi_3+\phi_1-\phi_2)+R_2R_3 \cos\chi_3-R_1R_2 \cos(\chi_3-\phi_1+\phi_3)}{R_1^2+R_3^2-2R_1R_3 \cos(\phi_1-\phi_3)}. \tag{65}$$

Appendix D: Solution for Flow Driven by a Top-Hat Surface Buoyancy Flux

For the case of a top-hat distribution of surface buoyancy flux, the transformed slope-normal buoyancy gradient is given by (32). Applying (48)–(50) and (32) in (23) and (25), and taking the inverse transforms, yields

$$\psi = -\int_{-\infty}^{\infty} \frac{\sin(kl/2)}{\pi k^2} R_1R_2R_3 \sum_{j=1}^{3} \mathrm{e}^{zR_j\cos\phi_j} C_j \mathrm{d}k, \tag{66}$$

$$b = \int_{-\infty}^{\infty} \frac{\sin(kl/2)}{\pi k^2} R_1R_2R_3 \sum_{j=1}^{3} \mathrm{e}^{zR_j\cos\phi_j} R_j D_j \mathrm{d}k, \tag{67}$$

where the planar wave functions C_j and D_j ($j = 1, 2, 3$) are given by:

$$C_1 \equiv \frac{R_2 R_3 \sin(\chi_1+\phi_1) - R_1 R_3 \sin(\chi_1+\phi_2) - R_1 R_2 \sin(\chi_1+\phi_3) + R_1^2 \sin(\chi_1-\phi_1+\phi_2+\phi_3)}{\left[R_1^2+R_3^2-2R_1R_3\cos(\phi_1-\phi_3)\right]\left[R_1^2+R_2^2-2R_1R_2\cos(\phi_1-\phi_2)\right]}, \tag{68}$$

$$C_2 \equiv \frac{R_1 R_3 \sin(\chi_2+\phi_2) - R_2 R_3 \sin(\chi_2+\phi_1) - R_1 R_2 \sin(\chi_2+\phi_3) + R_2^2 \sin(\chi_2+\phi_1-\phi_2+\phi_3)}{\left[R_2^2+R_3^2-2R_2R_3\cos(\phi_2-\phi_3)\right]\left[R_1^2+R_2^2-2R_1R_2\cos(\phi_1-\phi_2)\right]}, \tag{69}$$

$$C_3 \equiv \frac{R_3^2 \sin(\chi_3+\phi_1+\phi_2-\phi_3) - R_2 R_3 \sin(\chi_3+\phi_1) - R_1 R_3 \sin(\chi_3+\phi_2) + R_1 R_2 \sin(\chi_3+\phi_3)}{\left[R_1^2+R_3^2-2R_1R_3\cos(\phi_1-\phi_3)\right]\left[R_2^2+R_3^2-2R_2R_3\cos(\phi_2-\phi_3)\right]}, \tag{70}$$

$$D_1 \equiv -\frac{R_2 R_3 \cos(\chi_1+2\phi_1) - R_1 R_3 \cos(\chi_1+\phi_1+\phi_2) - R_1 R_2 \cos(\chi_1+\phi_1+\phi_3) + R_1^2 \cos(\chi_1+\phi_2+\phi_3)}{\left[R_1^2+R_3^2-2R_1R_3\cos(\phi_1-\phi_3)\right]\left[R_1^2+R_2^2-2R_1R_2\cos(\phi_1-\phi_2)\right]}, \tag{71}$$

$$D_2 \equiv \frac{R_1 R_3 \cos(\chi_2+2\phi_2) - R_2 R_3 \cos(\chi_2+\phi_1+\phi_2) + R_2^2 \cos(\chi_2+\phi_1+\phi_3) - R_1 R_2 \cos(\chi_2+\phi_2+\phi_3)}{\left[R_2^2+R_3^2-2R_2R_3\cos(\phi_2-\phi_3)\right]\left[R_1^2+R_2^2-2R_1R_2\cos(\phi_1-\phi_2)\right]}, \tag{72}$$

$$D_3 \equiv \mathrm{sgn}(k)\frac{R_1 R_2 \cos(\chi_3+2\phi_3) + R_3^2 \cos(\chi_3+\phi_1+\phi_2) - R_2 R_3 \cos(\chi_3+\phi_1+\phi_3) - R_1 R_3 \cos(\chi_3+\phi_2+\phi_3)}{\left[R_1^2+R_3^2-2R_1R_3\cos(\phi_1-\phi_3)\right]\left[R_2^2+R_3^2-2R_2R_3\cos(\phi_2-\phi_3)\right]}, \tag{73}$$

where $\chi_j \equiv kx + zR_j \sin\phi_j$.

References

Atkinson BW (1981) Meso-scale atmospheric circulations. Academic Press, London

Axelsen SL, Shapiro A, Fedorovich E, van Dop H (2010) Analytical solution for katabatic flow induced by an isolated cold strip. Environ Fluid Mech 10:387–414

Banta RM, Olivier LD, Gudiksen PH, Lange R (1996) Implications of small-scale flow features to modeling dispersion over complex terrain. J Appl Meteorol 35:330–342

Banta RM, Shepson PB, Bottenheim JW, Anlauf KG, Wiebe HA, Gallant A, Biesenthal T, Olivier LD, Zhu C-J, McKendry IG, Steyn DG (1997) Nocturnal cleansing flows in a tributary valley. Atmos Environ 31:2147–2162

Barros N, Borrego C, Toll I, Soriano C, Jiménez P, Baldasano JM (2003) Urban photochemical pollution in the Iberian peninsula: Lisbon and Barcelona airsheds. J Air Waste Manag Assoc 53:347–359

Bossert JE (1997) An investigation of flow regimes affecting the Mexico City region. J Appl Meteorol 36:119–140

Broder B, Gygax HA (1985) The influence of locally induced wind systems on the effectiveness of nocturnal dry deposition of ozone. Atmos Environ 19:1627–1637

Burkholder B, Shapiro A, Fedorovich E (2009) Katabatic flow induced by a cross-slope band of surface cooling. Acta Geophys 57:923–949

Clements WE, Archuleta JA, Hoard DE (1989) Mean structure of the nocturnal drainage flow in a deep valley. J Appl Meteorol 28:457–462

Cox HJ (1920) Weather conditions and thermal belts in the North Carolina mountain region and their relation to fruit growing. Ann Assoc Am Geogr 10:57–68

Dickerson MH, Gudiksen PH (1983) Atmospheric studies in complex terrain. Technical progress report N-1979 through FY-1983

Dunbar GS (1966) Thermal belts in North Carolina. Geogr Rev 56:516–526

Egger J (1981) On the linear two-dimensional theory of thermally induced slope winds. Beitr Phys Atmos 54:465–481

Fedorovich E, Shapiro A (2009a) Structure of numerically simulated katabatic and anabatic flows along steep slopes. Acta Geophys 57:981–1010

Fedorovich E, Shapiro A (2009b) Turbulent natural convection along a vertical plate immersed in a stably stratified fluid. J Fluid Mech 636:41–57
Fedorovich E, Nieuwstadt FTM, Kaiser R (2001) Numerical and laboratory study of a horizontally evolving convective boundary layer. Part I: Transition regimes and development of the mixed layer. J Atmos Sci 58:70–86
Fernando HJS (2010) Fluid dynamics of urban atmospheres in complex terrain. Annu Rev Fluid Mech 42: 365–389
Fernando HJS, Lee SM, Anderson J, Princevac M, Pardyjak E, Grossman-Clarke S (2001) Urban fluid mechanics: air circulation and contaminant dispersion in cities. Environ Fluid Mech 1:107–164
Finn D, Clawson KL, Carter RG, Rich JD, Allwine KJ (2008) Plume dispersion anomalies in a nocturnal urban boundary layer in complex terrain. J Appl Meteorol Climatol 47:2857–2878
Gohm A, Harnisch F, Vergeiner J, Obleitner F, Schnitzhofer R, Hansel A, Fix A, Neininger B, Emeis S, Schäfer K (2009) Air pollution transport in an alpine valley: results from airborne and ground-based observations. Boundary-Layer Meteorol 131:441–463
Grisogono B, Oerlemans J (2001) Katabatic flow: analytic solution for gradually varying eddy diffusivities. J Atmos Sci 58:3349–3354
Haiden T (2003) On the pressure field in the slope wind layer. J Atmos Sci 60:1632–1635
Hernández E, de las Parras J, Martín I, Rúa A, Gimeno L (1998) A field case study and numerical simulation of mountain flows with weak ambient winds. J Appl Meteorol 37:623–637
Hootman BW, Blumen W (1983) Analysis of nighttime drainage winds in Boulder, Colorado during 1980. Mon Weather Rev 111:1052–1061
Jeffrey DJ, Norman AC (2004) Not seeing the roots for the branches: multivalued functions in computer algebra. ACM SIGSAM Bull 38:57–66
King JA, Shair FH, Reible DD (1987) The influence of atmospheric stability on pollutant transport by slope winds. Atmos Environ 21:53–59
Kobayashi T, Mori M, Wakimizu K, Takeshita K (1994) An observational study of a thermal belt on hillsides. J Meteorol Soc Jpn 72:387–399
Koh RCY (1966) Viscous stratified flow toward a sink. J Fluid Mech 24:555–575
Kondo H (1984) The difference of the slope wind between day and night. J Meteorol Soc Jpn 62:224–233
Kossmann M, Sturman A (2004) The surface wind field during winter smog nights in Christchurch and coastal Canterbury, New Zealand. Int J Climatol 24:93–108
Lee SM, Fernando HJS, Princevac M, Zajic D, Sinesi M, McCulley JL, Anderson J (2003) Transport and diffusion of ozone in the nocturnal and morning planetary boundary layer of the Phoenix valley. Environ Fluid Mech 3:331–362
Lehner M, Gohm A (2010) Idealised simulations of daytime pollution transport in a steep valley and its sensitivity to thermal stratification and surface albedo. Boundary-Layer Meteorol 134:327–351
Low PS (1990) Katabatic winds in the lower Tamar valley, Tasmania. Il Nuovo Cimento C13:981–994
Lu R, Turco RP (1994) Air pollutant transport in a coastal environment. Part I: Two-dimensional simulations of sea-breeze and mountain effects. J Atmos Sci 51:2285–2308
Mahrt L (1982) Momentum balance of gravity flows. J Atmos Sci 39:2701–2711
Mahrt L, Larsen S (1982) Small scale drainage front. Tellus 34:579–587
Mahrt L, Vickers D, Nakamura R, Soler MR, Sun J, Burns S, Lenschow DH (2001) Shallow drainage flows. Boundary-Layer Meteorol 101:243–260
Mathews J, Walker RL (1970) Mathematical methods of physics. Benjamin/Cummings, Menlo Park
Millán MM, Estrela MJ, Badenas C (1998) Meteorological processes relevant to forest fire dynamics on the Spanish Mediterranean coast. J Appl Meteorol 37:83–100
Monti P, Fernando HJS, Princevac M, Chan WC, Kowalewski TA, Pardyjak ER (2002) Observations of flow and turbulence in the nocturnal boundary layer over a slope. J Atmos Sci 59:2513–2534
Nappo CJ, Shankar Rao K, Herwehe JA (1989) Pollutant transport and diffusion in katabatic flows. J Appl Meteorol 28:617–625
Oerlemans J (1998) The atmospheric boundary layer over melting glaciers. In: Holtslag AAM, Duynkerke PG (eds) Clear and cloudy boundary layers. Royal Netherlands Academy of Arts and Sciences, Amsterdam pp 129–153
Papadopoulos KH, Helmis CG, Soilemes AT, Kalogiros J, Papageorgas PG, Asimakopoulos DN (1997) The structure of katabatic flows down a simple slope. Q J R Meteorol Soc 123:1581–1601
Poulos G, Zhong S (2008) An observational history of small-scale katabatic winds in mid-latitudes. Geogr Compass 2:1798–1821
Prandtl L (1942) Führer durch die Strömungslehre. Vieweg and Sohn, Braunschweig
Segal M, Yu C-H, Arritt RW, Pielke RA (1988) On the impact of valley/ridge thermally induced circulations on regional pollutant transport. Atmos Environ 22:471–486

Shapiro A, Fedorovich E (2004a) Unsteady convectively driven flow along a vertical plate immersed in a stably stratified fluid. J Fluid Mech 498:333–352
Shapiro A, Fedorovich E (2004b) Prandtl number dependence of unsteady natural convection along a vertical plate in a stably stratified fluid. Int J Heat Mass Transf 47:4911–4927
Shapiro A, Fedorovich E (2006) Natural convection in a stably stratified fluid along vertical plates and cylinders with temporally-periodic surface temperature variations. J Fluid Mech 546:295–311
Shapiro A, Fedorovich E (2007) Katabatic flow along a differentially-cooled sloping surface. J Fluid Mech 571:149–175
Shapiro A, Fedorovich E (2008) Coriolis effects in homogeneous and inhomogeneous katabatic flows. Q J R Meteorol Soc 134:353–370
Sharples JJ (2009) An overview of mountain meteorological effects relevant to fire behaviour and bushfire risk. Int J Wildland Fire 18:737–754
Soriano C, Baldasano JM, Buttler WT, Moore K (2001) Circulatory patterns of air pollutants within the Barcelona air basin in a summertime situation: lidar and numerical approaches. Boundary-Layer Meteorol 98:33–55
Sturman AP (1987) Thermal influences on airflow in mountainous terrain. Prog Phys Geogr 11:183–206
Sturman AP, McGowan HA, Spronken-Smith RA (1999) Mesoscale and local climates in New Zealand. Prog Phys Geogr 23:611–635
Tanaka H, Tanimoto Y, Mikami T (1998) The relationship between double-thermal inversions and thermal belt in the Mt. Yatsugatake area, central Japan. Geographical reports of Tokyo Meteorological University 33, pp 21–31
Tyson PD (1968) Velocity fluctuations in the mountain wind. J Atmos Sci 25:381–384
Ueda H, Hori ME, Nohara D (2003) Observational study of the thermal belt on the slope of Mt. Tsukuba. J Meteorol Soc Jpn 81:1283–1288
Vergeiner I, Dreiseitl E (1987) Valley winds and slope winds—observations and elementary thoughts. Meteorol Atmos Phys 36:267–286
Whiteman CD (1990) Observations of thermally developed wind systems in mountainous terrain. In: Atmospheric processes over complex terrain. Meteorol monograph no. 45. American Meteorological Society, pp 5–42
Whiteman CD (2000) Mountain meteorology: fundamentals and applications. Oxford University Press, New York
Yakovenko SN, Thomas TG, Castro IP (2011) A turbulent patch arising from a breaking internal wave. J Fluid Mech 677:103–133
Yoshino MM (1984) Thermal belt and cold air drainage on the mountain slope and cold air lake in the basin at quiet, clear night. GeoJournal 8:235–250